New Journal of Physics
The open-access journal for physics

Anisotropic in-plane optical conductivity in detwinned $Ba(Fe_{1-x}Co_x)_2As_2$

A Dusza[1], A Lucarelli[1], A Sanna[2], S Massidda[2], J-H Chu[3], I R Fisher[3] and L Degiorgi[1,4]

[1] Laboratorium für Festkörperphysik, ETH—Zürich, CH-8093 Zürich, Switzerland
[2] Dipartimento di Fisica, Universitá degli Studi di Cagliari, IT-09042 Monserrato, Italy
[3] Geballe Laboratory for Advanced Materials and Department of Applied Physics, Stanford University, Stanford, CA 94305-4045, USA and Stanford Institute for Materials and Energy Sciences, SLAC National Accelerator Laboratory, 2575 Sand Hill Road, Menlo Park, CA 94025, USA
E-mail: degiorgi@solid.phys.ethz.ch

New Journal of Physics **14** (2012) 023020 (20pp)
Received 21 October 2011
Published 7 February 2012
Online at http://www.njp.org/
doi:10.1088/1367-2630/14/2/023020

Abstract. We study the anisotropic in-plane optical conductivity of detwinned $Ba(Fe_{1-x}Co_x)_2As_2$ single crystals for $x = 0$, 2.5 and 4.5% in a broad energy range (3 meV–5 eV) across their structural and magnetic transitions. For temperatures below the Neel transition, the topology of the reconstructed Fermi surface, combined with the distinct behavior of the scattering rates, determines the anisotropy of the low-frequency optical response. For the itinerant charge carriers, we are able to disentangle the evolution of the Drude weights and scattering rates and to observe their enhancement along the orthorhombic antiferromagnetic a-axis with respect to the ferromagnetic b-axis. For temperatures above the structural phase transition, uniaxial stress induces a finite in-plane anisotropy. The anisotropy of the optical conductivity, leading to significant dichroism, extends to high frequencies in the mid- and near-infrared regions. The temperature dependence of the dichroism at all dopings scales with the anisotropy ratio of dc conductivity, suggesting the electronic nature of the structural transition. Our findings bear testimony to a large nematic susceptibility that couples very effectively to the uniaxial lattice strain. In order to clarify

[4] Author to whom any correspondence should be addressed.

the subtle interplay of magnetism and Fermi surface topology we compare our results with theoretical calculations obtained from density functional theory within the full-potential linear augmented plane-wave method.

Contents

1. Introduction **2**
2. Experiment **4**
2.1. Samples 4
2.2. Technique 4
3. Results **6**
3.1. Reflectivity 6
3.2. Optical conductivity 8
3.3. Fits 10
4. Discussion **12**
5. Conclusions **19**
Acknowledgments **19**
References **19**

1. Introduction

In many unconventional superconductors including cuprates and Fe-based pnictides, superconductivity emerges from a complicated soup of competing phases in the normal state when magnetism is suppressed by doping, pressure or other external parameters [1, 2]. This multiplicity of phases includes nematicity, defined as the spontaneously broken C4 rotational symmetry of the square lattice, and a novel form of magnetism, arising from either orbital currents or antiferromagnetic fluctuations. In the Fe-based pnictide superconductors (for a review with a comprehensive reference list, see [3]), nematic correlations and antiferromagnetic fluctuations have also been recently connected with symmetry breaking competing phases. Inelastic neutron scattering experiments have revealed anisotropic magnetic excitations [4], coupled to the structural tetragonal–orthorhombic transition at T_s. This structural transition elongates the Fe–Fe distance in the ab-plane along the a-axis direction and contracts it along the perpendicular b-axis. It turns out that below the Neel temperature T_N ($\leqslant T_s$) the spins present ferromagnetic correlations along the shorter orthorhombic b-axis and antiferromagnetic ones along the longer a-axis [4]. The two-fold anisotropy is also evident in scanning tunneling microscopy measurements [5] and is further confirmed by angle-resolved photoemission spectroscopy (ARPES) data [6]. Furthermore, quantum oscillations in the parent compound reveal that the reconstructed Fermi surface comprises several pockets [7], the smallest of these being essentially isotropic in the ab-plane, while the other, larger pockets being much more anisotropic.

The first ARPES data [6], collected on crystals for which the incident beam size was comparable to the size of a single structural domain, motivated an intensive research activity also with probes for which any impact of the electronic anisotropy would be obscured by the formation of dense twin domains [8]. These adjacent microscopic domains are as small as a few microns with alternating orthorhombic a and b axes [9]. Uniaxial stress [9, 10] and in-plane magnetic field [11] have been employed so far to detwin the specimen. The former method, employed here, is superior in order to achieve an almost complete detwinning [8].

Recent ARPES measurements [12, 13] of detwinned single crystals of $Ba(Fe_{1-x}Co_x)_2As_2$ reveal a difference in orbital occupancy, consistent with a splitting of the d_{xz} and d_{yz} bands on cooling through T_s [12]. The diminishing orbital splitting upon Co-doping goes hand in hand with the monotonic decrease in the lattice orthorhombicity $[2(a-b)/(a+b)]$ [14].

Measurements of the dc resistivity as a function of temperature of the single-domain parent compounds $BaFe_2As_2$, $SrFe_2As_2$ and $CaFe_2As_2$ (i.e. the so-called 122 iron pnictides) reveal a modest in-plane dc anisotropy for temperatures below T_s, with the resistivity in the ferromagnetic direction larger than along the antiferromagnetic direction [10, 15, 16]. Contrary to the lattice orthorhombicity [14], the in-plane resistivity anisotropy initially increases with the concentration of the Co, Ni or Cu substituent, displaying a rather abrupt onset at a composition close to the start of the superconducting dome. The transport properties revert to an isotropic in-plane conductivity once the structural transition is completely suppressed upon doping [10, 17].

For temperatures above T_s, there is a remarkably large sensitivity to uniaxial pressure, leading to a persisting band splitting [12] and to a large induced in-plane resistivity anisotropy that is not observed for overdoped compositions [10]. Both thermodynamic and transport measurements do not support an additional phase transition above T_s for unstressed crystals, so that the induced anisotropy above T_s is the result of a large nematic susceptibility, rather than the presence of static nematic order.

Reflectivity measurements of detwinned single crystals using polarized light can provide important insight into the effects of the magnetic and structural transitions on the anisotropic charge dynamics and the electronic band structure. Indeed, the counterintuitive anisotropic behavior of $\rho(T)$ is also reflected in the finite-frequency response of the charge carriers as observed by the optical measurements reported in our previous work [18]. Optical measurements of detwinned single crystals of $Ba(Fe_{1-x}Co_x)_2As_2$ in the underdoped regime reveal large changes in the low-frequency metallic response on cooling through T_s and T_N together with a pronounced optical anisotropy (i.e. $\Delta\sigma_1(\omega) = \sigma_1(\omega, E \parallel a) - \sigma_1(\omega, E \parallel b)$, $\sigma_1(\omega)$ being the real part of the optical conductivity) at high frequencies, defining the linear dichroism [18]. The high-frequency dichroism, which is smaller for higher Co concentrations, clearly reveals that changes in the electronic structure are not confined to near the Fermi energy. Similar to dc transport and ARPES measurements, a pronounced optical anisotropy persists at temperatures above T_s for crystals held under uniaxial stress.

In this work, we expand in greater detail our broad spectral range characterization of the anisotropic optical conductivity of detwinned $Ba(Fe_{1-x}Co_x)_2As_2$ single crystals under uniaxial pressure. We extensively study the underdoped region at compositions with $x = 0$, $x = 0.025$ and $x = 0.045$ with light polarized along the in-plane orthorhombic a and b axes. Our previous paper in letter format [18] was devoted to the presentation of the punch lines and was mainly based on data of the parent compound ($x = 0$). Here, besides adding the findings for $x = 0.045$, we present the full set of data and their complete phenomenological analysis. Therefore, this review should serve the readers with a self-consistent and comprehensive presentation of our results. Complementary to the present full account of the collected data, we also wish to draw the attention of the readers to [8], where a comparison of selected optical findings with recent progress in determining the intrinsic in-plane electronic anisotropy as revealed by alternative techniques such as transport and photoemission is presented and discussed. Furthermore, in this experimental review, we directly compare our optical measurements with theoretical calculations obtained from density functional theory (DFT) within the full-potential

linear augmented plane wave (LAPW) method [19], in order to clarify the subtle interplay of magnetism and Fermi surface topology. Here, we explicitly and newly address the comparison of the band structure calculation and experimental data as a function of Co content in the underdoped regime.

2. Experiment

2.1. Samples

Single crystals of $Ba(Fe_{1-x}Co_x)_2As_2$ with $x = 0$, 2.5 and 4.5% were grown using a self-flux method [10]. The crystals have a plate-like morphology with thickness between 0.1 and 0.3 mm and with the c-axis perpendicular to the plane of the plates. Crystals were cut into a square shape, approximately 2 mm on the side, oriented such that below T_s the orthorhombic a/b axes are parallel to the sides of the square [10]. Detailed thermodynamic, transport and neutron scattering measurements for the studied dopings of $Ba(Fe_{1-x}Co_x)_2As_2$ provide evidence for structural, magnetic and superconducting phase transitions occurring at different temperatures [20, 21]: for $x = 0$, the coincident structural (tetragonal–orthorhombic) and magnetic transitions where the system forms antiferromagnetically ordered stripes occur at $T_s = T_N = 135$ K, whereas for $x = 0.025$ they develop at $T_s = 98$ K and $T_N = 92$ K, respectively. The compound with $x = 0.045$ undergoes first a structural transition at $T_s = 66$ K, then a magnetic transition at $T_N = 58$ K and finally a superconducting one at $T_c = 15$ K.

2.2. Technique

Single-domain specimens, achieved by the application of uniaxial pressure *in situ* [10], are crucial in order to reveal the intrinsic anisotropy of the orthorhombic phase. To this end, we have extended the basic cantilever concept originally developed for transport measurements in order to allow optical measurements under constant uniaxial pressure. The mechanical clamp (figure 1(a)) and the optical mask (figures 1(b) and (c)) attached on top of it in tight contact, forming the pressure device, were designed according to the following specific criteria [8, 18]: (i) the uniaxial stress is applied to the sample (S) by tightening a screw and drawing the clamp against the side of the crystal (figures 1(a) and (c)). Even though our clamp setup still lacks a precisely tunable pressure, the uniaxial stress was gradually increased (up to approximately 5 MPa [10]), so as to observe optical anisotropy. Uniaxial stress leads to a significantly larger population of domains oriented along a preferential direction, almost fully detwinning the crystals (with an estimated relative volume fraction of about 90% [8]). It turns out that the shorter ferromagnetic b-axis is oriented along the direction of the applied stress. (ii) The major axis of the tightening screw lies nearby and parallel to the surface of the sample so that the shear- and thermal-stress effects are minimized. The thermal expansion ΔL of the tightening screw, exerting the uniaxial pressure, can be estimated to be of the order of $\Delta L = \alpha L \, dT = 20 \, \mu$m (for screw length $L = 5$ mm, the typical metallic thermal expansion coefficient $\alpha = 2 \times 10^{-5}$ K^{-1} and thermal excursion $dT = 200$ K). This corresponds to a relative variation of about 0.4%. By reasonably assuming $\Delta L/L = \Delta p/p$, the influence of thermal expansion effects is then negligible. (iii) The (001) facet of the single-domain samples remains exposed, allowing optical reflectivity measurements. (iv) The optical mask guarantees data collection on the surfaces of the same dimension for S and reference mirror (M) and therefore on equivalent flat spots.

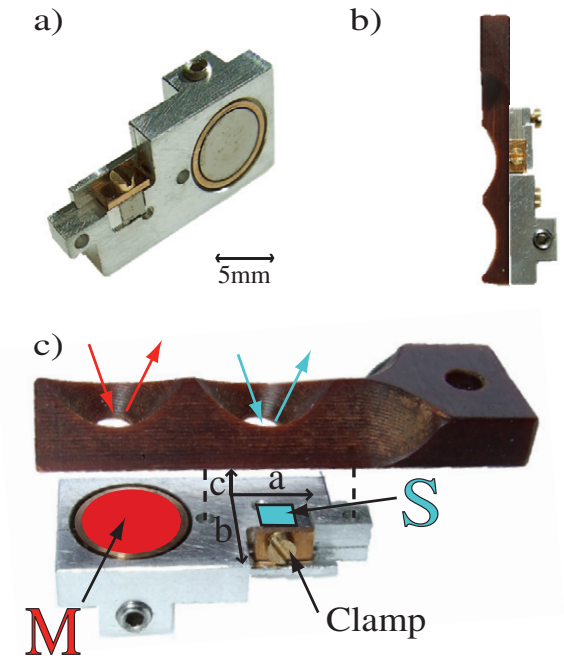

Figure 1. Sample-holder setup including a mechanical clamp (a) and an optical mask (b, c). Uniaxial pressure is applied parallel to the *b*-axis of the sample (S) by drawing the clamp against the side surface of the crystal (a, c). The optical mask, attached in tight contact with the clamp device, shapes identically incident and reflected light beams for the tungsten reference mirror M (red arrows) and S (light blue arrows). For the IR range the tungsten mirror guarantees a shiny and superior optical surface.

The reflectivity ($R(\omega)$) at room temperature was first collected from different spectrometers such as the Bruker IFS48 for the mid-infrared (MIR, 500–4000 cm^{-1}) and near-infrared (NIR; 4000–7000 cm^{-1}) measurements and a PerkinElmer Lambda 950 capable of measuring absolute reflectivity from NIR up to the ultraviolet (UV) range, i.e. 3200–4.8 $\times$ 10^4 cm^{-1}. The detwinning device was then placed inside our cryostat and finely aligned within the optical path of the Fourier transform infrared Bruker Vertex 80v interferometer by using a micrometer. This way, we could carry out optical measurements of $R(\omega)$ at different temperatures in the spectral range from the far-infrared (FIR; $\omega < 400\,\mathrm{cm}^{-1}$) up to the MIR, i.e. between 30 and 6000 cm^{-1}. The lowest trustable energy value in FIR may change within the 30–80 cm^{-1} energy interval, depending on the surface quality of the specimen. Light in all spectrometers was polarized along the *a* and *b* axes of the detwinned samples.

The real part $\sigma_1(\omega)$ of the optical conductivity was obtained via the Kramers–Kronig transformation of $R(\omega)$ by applying suitable extrapolations at low and high frequencies. For the $\omega \to 0$ extrapolation, we made use of the Hagen–Rubens (HR) formula ($R(\omega) = 1 - 2\sqrt{\frac{\omega}{\sigma_{\mathrm{dc}}}}$), inserting the dc conductivity values (σ_{dc}) from [10], while above the upper frequency limit $R(\omega) \sim \omega^{-s}$ ($2 \leqslant s \leqslant 4$) [22]. The merging of the measured data with the HR extrapolation was performed in the energy interval between 30 and 70 cm^{-1}.

Several precautions were taken in order to avoid experimental artifacts: (i) the polarizers chosen for each measured frequency range have an extinction ratio greater than 200, thus

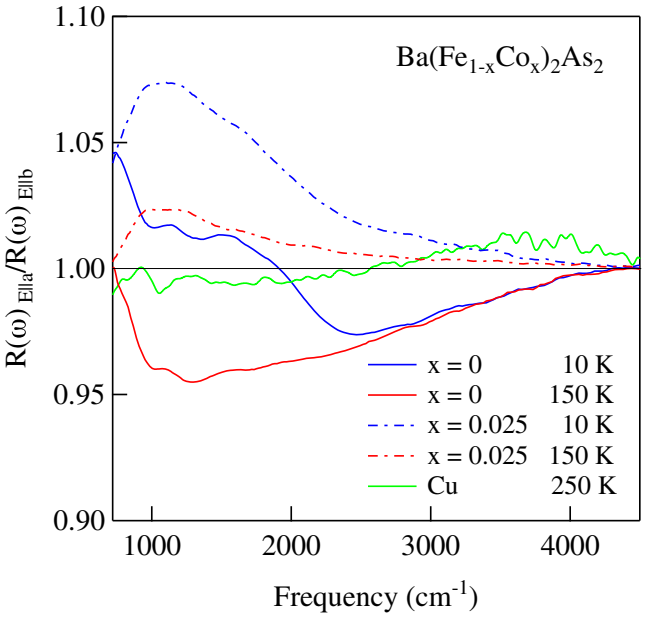

Figure 2. Reflectivity ratio $R(\omega)_{E\|a}/R(\omega)_{E\|b}$ measured above and below T_s along the a- and b-axis polarization directions for $Ba(Fe_{1-x}Co_x)_2As_2$ with $x = 0$ and 0.025 compared with the same ratio for a Cu sample of equivalent surface dimensions and thickness.

reducing leakages below our 1% error limit. (ii) As control measurements for the detwinning setup, we collected at different temperatures the optical reflectivity of a Cu sample of comparable surface dimensions and thickness with respect to the pnictide crystals and under equivalent uniaxial pressure. As expected, we could not observe any polarization dependence of the Cu reflectivity from room temperature down to 10 K (see e.g. the data at 250 K in figure 2). The Cu test measurements set to about 1–2% the higher limit of the polarization dependence due to any possible experimental artifacts (i.e. bended surfaces, leakage of the polarizers, etc), which is notably lower than the anisotropy ratio measured for the iron-pnictides (figures 2 and 3). (iii) Measurements with unpolarized light of twinned specimens (i.e. within the pressure device but without applying uniaxial stress) were first performed, in order to consistently recover the same spectra previously presented in [23]. (vi) We checked the alignment conditions between M and S (figure 1(c)) by imaging at 300 K a red laser point source on both spots.

3. Results

3.1. Reflectivity

The three investigated compositions display a similar optical response, but their polarization and temperature dependences show small yet significant differences as we clarify in the presentation and discussion of our results below. Figure 3 presents the optical reflectivity $R(\omega)$ in the whole measured frequency range of detwinned $Ba(Fe_{1-x}Co_x)_2As_2$ ($x = 0$, $x = 0.025$ and $x = 0.045$) at different temperatures and for the two polarization directions $E \| a$ and $E \| b$. As already recognized in the twinned (i.e. unstressed) specimens (for a review of optical results on

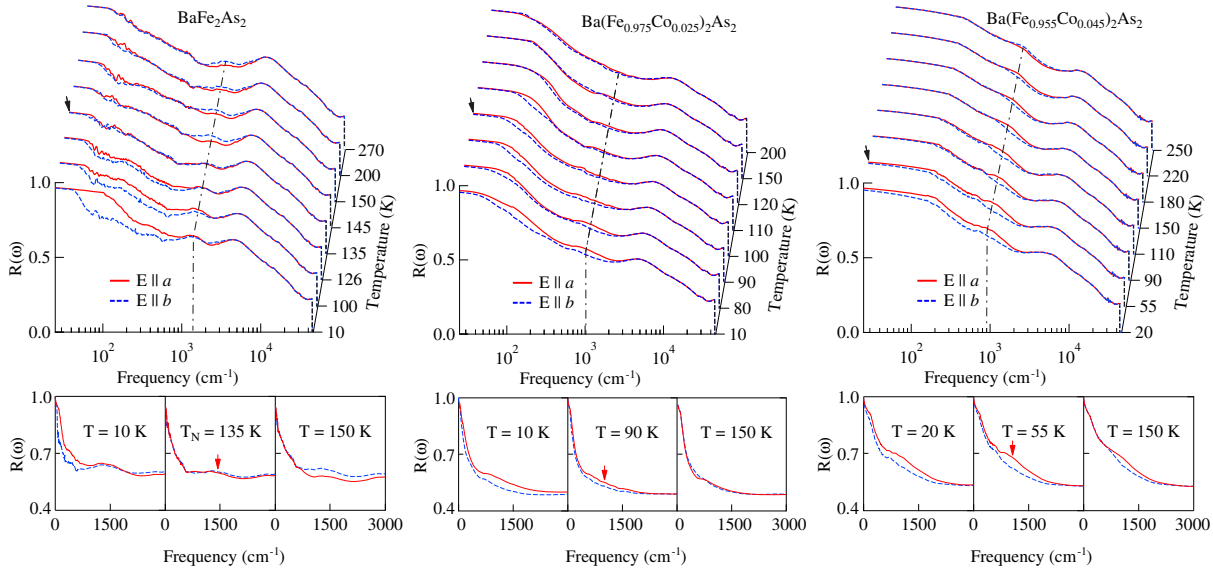

Figure 3. Temperature dependence of the optical reflectivity of detwinned $BaFe_2As_2$ (a), $Ba(Fe_{0.975}Co_{0.025})_2As_2$ (b) and $Ba(Fe_{0.955}Co_{0.045})_2As_2$ (c) in the whole measured spectral range for two polarizations, parallel to the a-axis direction ($E \parallel a$, red solid line) or perpendicular to it ($E \parallel b$, blue dashed line). The black arrows indicate $R(\omega)$ at the temperature close to the structural phase transition at T_s. The dashed-dotted line (top panels) and red arrows (bottom panels) indicate the center of the MIR band at all temperatures and close to T_N, respectively.

unstressed samples with a comprehensive reference list, see [23]), $R(\omega)$ gently increases from the UV to the MIR region displaying an overdamped-like behavior. Below the MIR energy range, $R(\omega)$ gets progressively steeper with a sharp upturn at frequencies lower than 200 cm^{-1} (figure 3). Close to zero frequency, $R(\omega)$ agrees with the HR extrapolations calculated with the σ_{dc} values from [10]. For all measured dopings we observed a polarization and temperature dependence of $R(\omega)$ from the FIR up to the MIR–NIR range, while between 5000 and 6000 cm^{-1} the $R(\omega)$ spectra merge together. The optical anisotropy is rather pronounced at low temperatures in the FIR region, when approaching the zero-frequency limit. Interestingly for $x = 0$, $R(\omega)$ increases with decreasing temperature along the a-axis, in agreement with the metallic character of the dc transport properties [10]. In contrast, at low temperatures along the b-axis, there is first a depletion of $R(\omega)$ in the FIR energy range below 700 cm^{-1} and then a steeper upturn below 100 cm^{-1}, consistently merging with the HR extrapolation. While somehow common to all compositions, this depletion is less pronounced at higher doping levels such as $x = 0.025$ and $x = 0.045$ when entering the magnetic ordered phase at $T < T_N$ (figures 3(b) and (c), respectively), similarly to what has been previously observed in the twinned specimens [23].

The anisotropy, discussed so far in the dc limit of $R(\omega)$ at low temperatures, persists up to temperatures well above all phase transitions for the crystals held under uniaxial pressure, predominantly in the MIR–NIR region than in the FIR one. The black arrow in figure 3

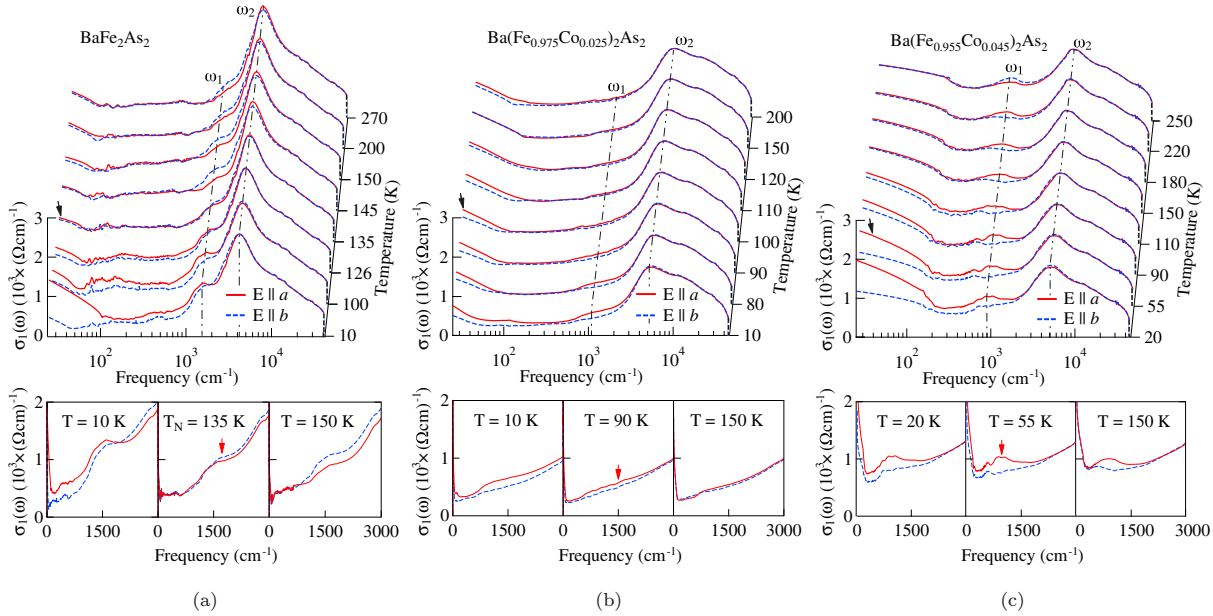

Figure 4. Temperature dependence of the optical conductivity of detwinned $BaFe_2As_2$ (a), $Ba(Fe_{0.975}Co_{0.025})_2As_2$ (b) and $Ba(Fe_{0.955}Co_{0.045})_2As_2$ (c) in the whole measured spectral range for two polarizations, parallel to the a-axis direction ($E \parallel a$, red solid line) or perpendicular to it ($E \parallel b$, blue dashed line). The black arrows indicate $\sigma_1(\omega)$ at the temperature close to the structural phase transition at T_s, while the red arrows (bottom panels) indicate the center of the MIR band close to T_N. The dashed-dotted and dashed double-dotted lines (top panels) mark the frequency ω_1 and ω_2 (see text).

highlights the $R(\omega)$ spectra collected at temperatures close to the respective T_s. The MIR band centered at about 1500 cm^{-1} (dotted-dashed lines and red arrow in figure 3) is of particular interest for both its temperature and polarization dependence. For $x = 0$, we observe an interchange in the polarization dependence of $R(\omega)$ with decreasing temperature (figure 3(a), bottom panels). Such an interchange exactly occurs at the coupled magnetic and structural phase transition at 135 K. At higher doping levels ($x = 0.025$ and $x = 0.045$) the MIR band observed at 1500 cm^{-1} for $x = 0$ is shifted towards lower frequencies (red arrows in bottom panels of figure 3). Above 150 K the anisotropy of $R(\omega)$ in the MIR region is strongly reduced, but differently from the parent compound the a-axis spectrum of $x = 0.025$ and $x = 0.045$ is constantly above the b-axis one at all temperatures (figures 3(b) and (c), bottom panels).

3.2. Optical conductivity

Figure 4 shows the real part $\sigma_1(\omega)$ of the optical conductivity of detwinned $Ba(Fe_{1-x}Co_x)_2As_2$ ($x = 0$, $x = 0.025$ and $x = 0.045$) for different temperatures along both polarization directions. In the visible and UV energy interval $\sigma_1(\omega)$ is characterized by polarization-independent broad absorption bands which overlap with a dominant NIR contribution peaked at about 5000 cm^{-1}. Consistently with previous measurements on twinned samples [23], these components of $\sigma_1(\omega)$

are generally ascribed to the electronic interband transitions. These features in the UV–NIR range are not substantially altered by changing temperature, polarization or doping level.

As already observed for $R(\omega)$, the temperature- and doping-dependent optical anisotropy in $\sigma_1(\omega)$ is mainly evident in the FIR and MIR regions. In the FIR region, there is a strong polarization dependence of the itinerant charge carriers contribution to $\sigma_1(\omega)$. Along the a-axis, $\sigma_1(\omega)$ shows a more pronounced metallic behavior, which gets enhanced below T_N. Along the b-axis $\sigma_1(\omega)$ below T_N is depleted due to the formation of a pseudogap, prior to displaying a metallic-like upturn for $\omega \to 0$. It might be speculated at this point that the b-axis response dominates the overall depletion of the optical conductivity, first observed in the magnetic state of the twinned samples [23]. As formerly observed for the twinned samples this depletion of $\sigma_1(\omega)$ along the b-axis is less evident when increasing the doping [23]. The reduced pseudogap-like feature in the optical conductivity upon doping may go hand in hand with the monotonic decrease of the orthorhombicity with increasing Co content [14].

The strong absorption peak dominating $\sigma_1(\omega)$ at about $5000\,\mathrm{cm}^{-1}$ develops into a pronounced shoulder on its MIR frequency tail at about $1500\,\mathrm{cm}^{-1}$. As anticipated in the presentation of the $R(\omega)$ data, this latter MIR band in $\sigma_1(\omega)$ shows a strong polarization and doping dependence, as highlighted in figure 4 (bottom panels). One recognizes again the already mentioned interchange in the polarization dependence when crossing the structural transition for $x = 0$ and its absence at higher dopings. Above T_N in the MIR range, $\sigma_1(\omega)$ of $x = 0.025$ and $x = 0.045$ along the a-axis direction is above the b-axis values and remains constantly above it also below T_N (top and bottom panels of figures 4(b) and (c), respectively). Interestingly enough, for increasing doping the maximum of the MIR band shifts to lower frequencies, indicating that the MIR band is significantly affected by the doping (dotted-dashed lines in the top panels and red arrows in the bottom panels of figure 4).

At this stage, it is worth mentioning that recent measurements, probing the in-plane optical anisotropy of $BaFe_2As_2$ [24], broadly confirm our findings at high frequencies for $x = 0$, as described above. There are some differences among the two investigations, as well. While we do observe in our spectra a sharp phonon mode along the b-direction at the same frequency as in [24], its intensity, however, is much weaker so that it can be barely observed in the layout of figures 3 and 4. This may be due to an insufficient resolution ($2\,\mathrm{cm}^{-1}$ in our setup) or may possibly indicate a more effective screening by the itinerant charge carriers in our specimen. The temperature dependence of the optical spectra in the low-frequency metallic part also differs among the two investigations, being, however, consistent with their respective dc properties. The data of [24] indicate a temperature dependence of the optical response consisting in the opening of a (pseudo)gap-like feature and a progressive narrowing of the residual Drude component for both polarization directions. Nonetheless, such a narrowing at $T < 50\,\mathrm{K}$ is inferred from an ad hoc extrapolation of the reflectivity spectra below $50\,\mathrm{cm}^{-1}$ (so that it falls outside of their measured spectral range). While a different degree of detwinning cannot be excluded *a priori* between the two sets of data, the possible reason for the difference in the electrodynamic response at low frequencies and temperatures along the a-axis may lie in the fact that our measurements were carried out on an as-grown sample, while Nakajima *et al* used an annealed specimen, for which the anisotropy below T_s in the dc transport is almost totally absent.

Even though we will return later on to the comparison between experiment and theory, we can already anticipate that *ab initio* calculations based on DFT as well as dynamical mean-field theory (DMFT) [19, 25, 26] are rather powerful instruments in order to reproduce in a fairly detailed fashion the anisotropic response in the magnetic state. On the one hand, DMFT

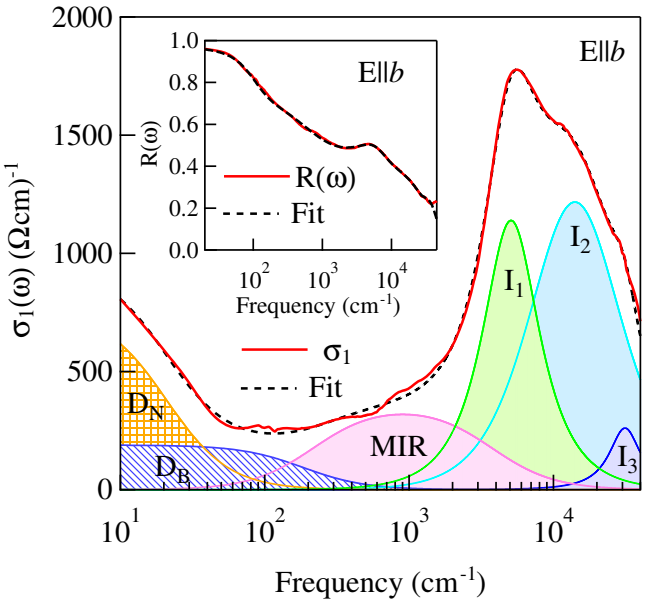

Figure 5. Optical conductivity along the b-axis at 10 K of detwinned $Ba(Fe_{0.975}Co_{0.025})_2As_2$ compared with the total Drude–Lorentz fit (black dashed line) and the corresponding components: the narrow (D_N) and broad (D_B) Drude terms, the MIR band and the oscillators (I_1, I_2, I_3) fitting the interband transitions. The inset shows a comparison of the measured reflectivity $R(\omega)$ and the resulting fit.

calculations addressing the role of correlation effects were able to show that the anisotropic charge dynamics cannot be treated solely by the local spin density approximation [25]. On the other, DFT calculations of the optical conductivity [19] catch most of the observed experimental features. A particularly great success of this latter approach consists in the reproduction of the anisotropic magnetic peak located at about 0.2 eV (1600 cm^{-1}), which was ascribed to antiferromagnetically ordered stripes [19]. The optical anisotropy, as observed experimentally, was even shown to agree with the solution of a three-dimensional five-orbital Hubbard model using the mean-field approximation in the presence of both orbital and magnetic order [27]. Moreover, it has been recently pointed out that interband transitions, the relevance of which is manifested by first-principle calculations, give a non-negligible contribution already in the infrared region, spanning the experimental energy interval of the MIR band [28].

3.3. Fits

In order to study the various contributions shaping the optical conductivity at different energies, we apply the well-established phenomenological Drude–Lorentz approach. Consistent with our previous investigations on twinned samples [23], we ascribe two Drude contributions (one narrow and one broad) to the effective metallic part of $\sigma_1(\omega)$ and a series of Lorentz harmonic oscillators (h.o.) for all excitations (phononic and electronic) at finite frequencies. Figure 5 presents all fitting components for $x = 0.025$ along the b-axis direction measured at 10 K, acting here as a representative example. The narrow Drude term is relevant at very low frequencies and it is obviously tied to the necessary HR extrapolation of $R(\omega)$ for $\omega \to 0$. The broad one acts

as a background of $\sigma_1(\omega)$ and dominates the optical conductivity up to the MIR energy interval. As we shall elaborate later on, both Drude terms contribute to the total dc conductivity. Besides the Drude terms, we consider one broad h.o. for the temperature-dependent MIR band and three broad h.o.'s (I_1, I_2 and I_3 in figure 5) for the strong absorption featuring the broad peak centered at about 5000 cm^{-1}. This fitting procedure is by now widely used and pretty well established among several groups, as nicely summarized in the seminal work by Wu *et al* [29].

The use of two Drude components in the fit procedure phenomenologically mimics the multi-band scenario and implies the existence of two electronic subsystems as revealed for an ample range of iron-pnictide compounds [3]. Even for the $x = 0$ compound, which is characterized by the largest Fermi surface reconstruction in the magnetic state, the two-Drude-terms fitting procedure guarantees a superior reproducibility of the optical conductivity as a function of temperature. In this context, it is also worth noting that given this fit procedure (figure 5) and keeping in mind that the resonance frequencies of the MIR band and NIR absorption are set by the shoulder at about 1500 cm^{-1} and by the peak at about 5000 cm^{-1} in $\sigma_1(\omega)$, respectively, the remaining Drude terms are consequently determined and depend exclusively on the temperature dependence of the data.

We are aware of the fact that various alternative fitting procedures could be applied. For instance, the MIR band may be described by a variable number of harmonic oscillators. We choose to describe it with one single h.o., in order to keep the number of fit components as low as possible. We can generally state that the decomposition of $\sigma_1(\omega)$ treated here (figure 5) allows a systematic reproduction of the optical conductivity at any doping level and temperature, establishing a robust trend in the evolution of the fitting parameters with respect to both variables. We thus favor a fitting procedure, which keeps the type and number of components identical above and below T_s for both polarization directions. This contrasts with the fits by Nakajima *et al* [24], who employ a similar fitting procedure above T_s, but change it below T_s as far as both the type and number of components are concerned.

Therefore, the complex dielectric function $\tilde{\varepsilon} = \varepsilon_1(\omega) + \mathrm{i}\varepsilon_2(\omega)$ can be expressed as follows [22]:

$$\tilde{\varepsilon} = \varepsilon_\infty - \frac{\omega_{\mathrm{PN}}^2}{\omega^2 - \mathrm{i}\omega\Gamma_{\mathrm{N}}} - \frac{\omega_{\mathrm{PB}}^2}{\omega^2 - \mathrm{i}\omega\Gamma_{\mathrm{B}}} + \frac{S_{\mathrm{MIR}}^2}{\omega_{\mathrm{MIR}}^2 - \omega^2 - \mathrm{i}\omega\gamma_{\mathrm{MIR}}} + \sum_{j=1}^{3} \frac{S_j^2}{\omega_j^2 - \omega^2 - \mathrm{i}\omega\gamma_j}, \tag{1}$$

where ε_∞ is the optical dielectric constant, ω_{PN}^2, ω_{PB}^2 and Γ_{N}, Γ_{B} are in turn the squared plasma frequencies, defined as $\omega_{\mathrm{P}}^2 = \frac{4\pi e^2 n}{m^*}$, and the widths of the narrow and broad Drude peaks. The latter parameters represent the scattering rates of the itinerant charge carriers, of which n, m^* and e are then the electron density, effective mass and charge, respectively. The parameters of the jth Lorenz h.o. as well as those of the MIR band are: the center-peak frequency (ω_j and ω_{MIR}), the width (γ_j and γ_{MIR}) and the mode strength (S_j^2 and S_{MIR}^2). The fit constraints are such that the measured reflectivity and the real part of the optical conductivity are simultaneously reproduced by the identical set of fit components as well as fit parameters for both quantities [23]. The upper boundary for the temperature dependence of the optical conductivity is found to be close to the NIR peak in $\sigma_1(\omega)$ at about 5000 cm^{-1}. Thus, for all temperatures and dopings we fit $R(\omega)$ and $\sigma_1(\omega)$ by varying the parameters for both Drude terms, the MIR band and the I_1 h.o., while keeping constant the parameters associated with the two high-frequency oscillators I_2 and I_3. It is worth mentioning that the optical dielectric constant (ϵ_∞) is independent of temperature as well as isotropic for each doping and ranges between 1.2 and 1.4 as a function of doping. This indicates that the whole electronic anisotropy is exhausted within the measured spectral

range and it is basically accounted for by the fit components displayed in figure 5. Moreover, our fitting procedure (figure 5) was adopted to all studied compositions, except for $x = 0$ along the b-axis, where for the MIR band we added one more component, in order to achieve a better fit quality. This additional component is purely phenomenological and does not have a specific assignment. We checked that this fit variation has negligible impact on the overall trend of the extracted parameters. The remarkable agreement of the fitting results with the measured reflectivity and optical conductivity (see e.g. figure 5) further demonstrates the overall good quality of our fits. Therefore, we are confident that our fit procedure is a valuable route among many in order to identify meaningful and consistent trends in relevant physical parameters.

4. Discussion

We can first exploit our phenomenological fits from the perspective of a so-called spectral weight (SW) analysis, represented by the squared plasma frequencies and mode strengths of the Drude terms and Lorentz h.o.'s, respectively. The Drude–Lorentz procedure thus supplies a suitable tool in order to follow the redistribution of SW in selected energy intervals and tells us how the same SW is reshuffled among the various components as a function of temperature. Moreover, we can selectively disentangle the SW distribution for both polarizations, thus going beyond the average view discussed in [23]. Of particular interest is the total Drude weight given by $\mathrm{SW_{Drude}} = \omega_{\mathrm{PN}}^2 + \omega_{\mathrm{PB}}^2$. Furthermore, we consider the SW encountered in the MIR band and electron interband transitions, defined as $\mathrm{SW_{MIR}} = S_{\mathrm{MIR}}^2$ and $\mathrm{SW_{Int}} = \sum_{j=1}^{3} S_j^2$, respectively. The total SW is then given by the area under the conductivity spectrum and can be expressed as [22]: $\mathrm{SW_{Total}} = \mathrm{SW_{Drude}} + \mathrm{SW_{MIR}} + \mathrm{SW_{Int}}$. Due to the high fit-quality of $\sigma_1(\omega)$ for the chosen components, $\mathrm{SW_{Total}}$ is also equivalent to $\int_0^{\omega_c} \sigma_1(\omega)\,\mathrm{d}\omega$, where ω_c corresponds to a cutoff frequency and basically sets the upper frequency limit of our measurements. This implies that if $\mathrm{SW_{Total}}$ does not change with temperature within the energy interval between zero and ω_c, any redistribution of the SW will fully occur among the fitting components.

The lower panels of figure 6 show the temperature dependence of $\mathrm{SW_{Total}}$ and the SW associated with the two Drude terms, the MIR band and the three interband excitations (I_i). $\mathrm{SW_{Total}}$ stays constant with temperature along both polarization directions for all doping values, thus satisfying the f-sum rule [22]. When crossing the structural and magnetic transitions, the SW of the parent compound along the a-axis is redistributed from high to low frequencies, since the interband transition components lose weight in favor of the Drude and MIR band (bottom panel of figure 6(a)). In contrast, along the b-axis, the Drude term loses SW for $T < T_N$ in favor of the MIR band. At higher dopings ($x = 0.025$ and 0.045) the overall $\mathrm{SW_{Int}}$ shows less pronounced temperature dependence for both lattice directions. For these latter dopings, the SW variations with temperature mainly occur between the Drude terms and the MIR band. A suppression of SW at one fit component leads to the weight enhancement of the other. Summarizing, the total SW for the parent compound is conserved up to frequencies of the order of 6000 $\mathrm{cm^{-1}}$ for both polarizations, while the f-sum rule at higher dopings is already satisfied above the MIR band (i.e. approximately at 3000 $\mathrm{cm^{-1}}$).

The resulting temperature dependence of $\mathrm{SW_{Drude}}$, increasing along the a- but decreasing along the b-axis across T_N and T_s, is quite a general notion for all dopings (figure 6) but it is rather intriguing and unanticipated as well, the significance of which with respect to the dc transport properties will be addressed below. For the time being, it is worth emphasizing that the Drude weight anisotropy may strongly depend on the topology and morphology of

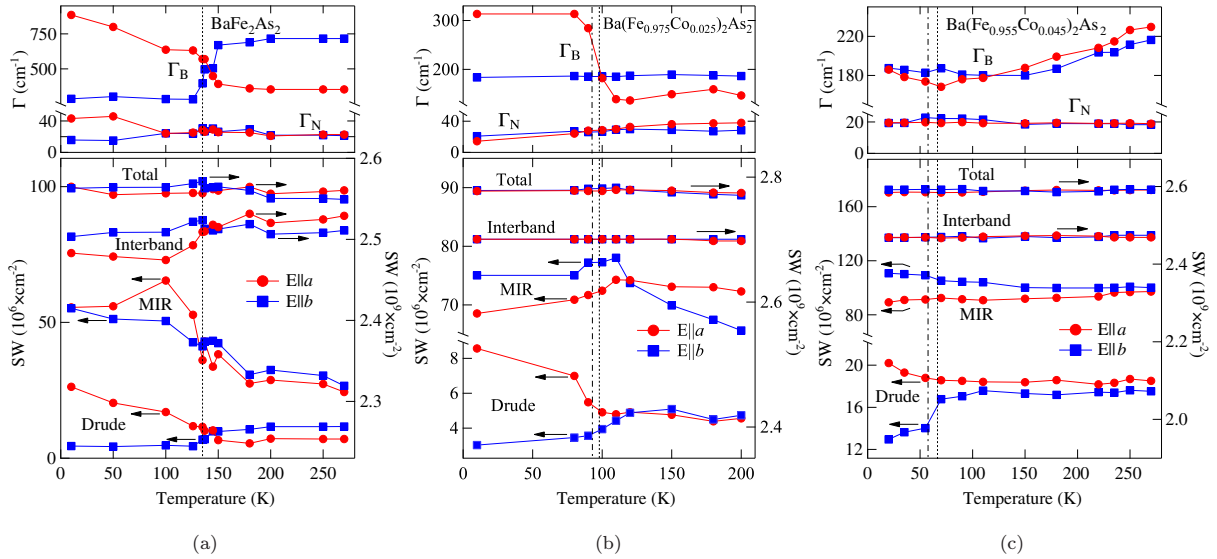

Figure 6. Temperature and polarization dependence of the widths for the broad (Γ_B) and narrow (Γ_N) Drude terms (top panels) and the spectral weight (SW) (bottom panels) for the Drude, the MIR and the interband components compared with the total SW obtained from the fits of $BaFe_2As_2$ (a), $Ba(Fe_{0.975}Co_{0.025})_2As_2$ (b) and $Ba(Fe_{0.955}Co_{0.045})_2As_2$ (c). The dotted and dotted-dashed lines indicate the structural and magnetic transitions at T_s and T_N, respectively.

the reconstructed Fermi surface below T_s (i.e. anisotropy of the Fermi velocity), as evinced from a five-band Hamiltonian at the mean-field level [30]. Nakajima *et al* [24] analyze the integrated SW but do not sort out its redistribution among the fitting components as a function of temperature. A tentative comparison can be proposed for $x = 0$ only. Keeping in mind the already quoted difference between annealed and as-grown samples, the data of [24] call for a piling up of SW both along the a- and b-axis in very narrow Drude resonances (mostly outside the measured energy intervals), followed by its depletion at FIR frequencies as a consequence of the gap opening below T_s. The latter SW depletion is stronger for $E \parallel b$ than for $E \parallel a$ [24]. Our detailed analysis, indicating a substantial shift of SW into the MIR band and a related suppression in the overall Drude components for $E \parallel b$, may be certainly compatible with the outcome of [24], less so for $E \parallel a$.

Of interest is also for $x = 0$ the temperature-independent total Drude weight, which is larger along the b-axis than along the a-axis for $T > T_s$, thus inverting the polarization dependence observed below T_s. This astonishing behavior for $x = 0$ might be compatible with a recent multi-orbital model [27]. However, given the ARPES results [12], showing that the band splitting diminishes with increasing temperature, one would have eventually anticipated that the Drude weight gets indeed isotropic above T_s, which is not the case in our data for $x = 0$. Nonetheless, the Drude weight anisotropy above T_s is suppressed upon doping (figure 6). Experimentally, such a trend of SW_{Drude} remains to be verified under controlled uniaxial pressure conditions, while theoretically it awaits confirmation within doping-dependent models.

From the width at half-maximum of the Drude resonance, we can extract the scattering rates of the itinerant charge carriers. The broad (Γ_B) and narrow (Γ_N) Drude widths for $x = 0$, 0.025 and 0.045 are shown in the top panels of figure 6. As previously stated, the

narrow Drude term must be considered with caution, being mainly the consequence of the low-frequency HR extrapolation. Nonetheless, Γ_N either follows the same behavior as Γ_B ($x = 0$) or is just temperature independent ($x = 0.025$ and 0.045). The behavior of Γ_B allows more robust conclusions, since it relates to a Drude component covering the measured energy interval. We limit the present discussion to the anisotropic behavior of the scattering rates as a function of doping in detwinned specimens; see [23] and [29] for the analysis of Γ_N and Γ_B with respect to the dc transport properties in twinned samples. An anisotropy in the scattering rate is most evident for $x = 0$ and $x = 0.025$. For $x = 0$ the Drude scattering rates Γ_N and Γ_B increase along the a-axis and decrease along the b-axis for decreasing temperatures across the phase transitions. Above T_s for $x = 0$, Γ_N along both axes saturates to the identical constant value, while Γ_B displays an inversion in the polarization dependence with respect to the situation below T_s (figure 6, upper panel), before saturating to temperature-independent values. The strong decrease of Γ_B (as well as of Γ_N) for $E \parallel b$ at $T < T_s$ is, furthermore, compatible with statements in [24]. For $x = 0.025$ only Γ_B along the a-axis undergoes a sudden incremental change at T_N, while all other scattering rates remain almost constant. Γ_B above T_s is switched with respect to below T_s between the two polarization directions, similarly to the case for $x = 0$ yet less pronounced. For $x = 0.045$ the Γ_B scattering rate for both polarizations displays a more metallic behavior with decreasing temperature above T_N and an almost negligible polarization dependence. Below T_N there is a weak upturn to higher values, particularly along the a-axis. Γ_N remain constant at all temperatures and for both directions.

The overall temperature dependence of the scattering rates below T_N as evinced from the analysis of the optical response is expected with respect to the well-established magnetic order [4]. Particularly for $x = 0$ and $x = 0.025$, the larger scattering rates along the elongated antiferromagnetic a-axis than along the shorter ferromagnetic b-axis for temperatures below T_N may arise because of reduced hopping along the a- than along the b-axis or of scattering from spin fluctuations with large momentum transfer (i.e. by incoherent spin waves) [31, 32]. The anisotropic scattering rate in the paramagnetic state, at least for $x = 0$ and $x = 0.025$, might also be in agreement with predictions based on the interference between scattering by impurities and by critical spin fluctuations in the Ising nematic state [33]. Similarly to our previous discussion on the Drude weight, we shall caution the reader that the trend in the scattering rates, particularly above T_s, as well as their doping dependence should also be verified with tunable uniaxial pressures, in order to guarantee equal experimental conditions. A comprehensive theoretical framework, approaching different temperature regimes and considering the impact of doping, is also desired.

Having determined the two parameters governing the dc transport properties, it is worth pursuing the compelling comparison between the temperature dependence of the optical anisotropy and the anisotropy ratio of the dc transport properties, defined as $\frac{\Delta\rho}{\rho} = \frac{2(\rho_b - \rho_a)}{(\rho_b + \rho_a)}$ (figure 7) [8, 18, 31]. From the Drude terms, fitting the effective metallic contribution of $\sigma_1(\omega)$ over a finite energy interval, we can estimate the dc limit of the conductivity ($\sigma_0^{\rm opt} = (\omega_p^N)^2/4\pi\Gamma_N + (\omega_p^B)^2/4\pi\Gamma_B$) more precisely than simply extrapolating $\sigma_1(\omega)$ to zero frequency. Indeed, relying on the $\sigma_1(\omega \to 0)$ limit would lead to less reliable estimation of the dc conductivity, because of the noisy extrapolation of $\sigma_1(\omega)$ from the Kramers–Kronig results below $10\,\mathrm{cm}^{-1}$. The anisotropy of the Drude parameters anticipates the sensitiveness to symmetry breaking phases of Fermi surface-related quantities such as the dc transport properties (figure 7). The anisotropy ratio $\frac{\Delta\rho^{\rm opt}}{\rho}$, reconstructed from the optical data, is thus compared in figure 7 to the equivalent quantity from the transport investigation. On a general ground, the

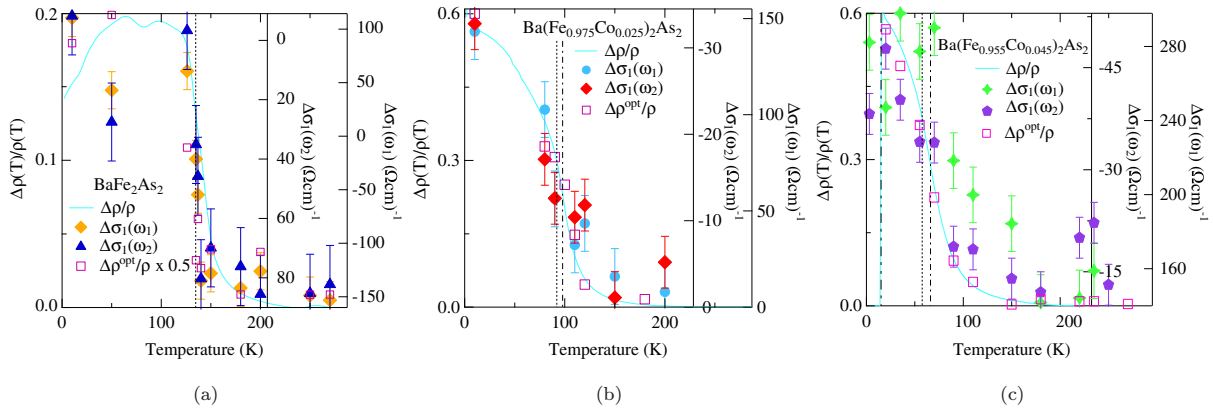

Figure 7. Temperature dependence of the dichroism $\Delta\sigma_1(\omega)$ of $BaFe_2As_2$ (a), $Ba(Fe_{0.975}Co_{0.025})_2As_2$ (b) and $Ba(Fe_{0.955}Co_{0.045})_2As_2$ (c) at ω_1 and ω_2 (figure 4) compared to $\frac{\Delta\rho}{\rho}$ obtained from the dc transport data, as well as from the Drude terms in $\sigma_1(\omega)(\Delta\rho^{\rm opt}/\rho)$. The vertical dotted-dashed, dotted and double-dotted-dashed lines mark the structural, magnetic and superconducting phase transitions at T_s, T_N and T_c, respectively.

enhancement (depletion) of the total Drude SW occurring along the a (b)-axis outweighs the (large at some compositions) anisotropy in the scattering rates (figure 6) that develops below T_N towards the effect on the dc transport properties (figure 7). The agreement in terms of $\frac{\Delta\rho}{\rho}$ between the optical and dc investigations is outstanding for $x = 0.025$ and good for 0.045 at all temperatures. For $x = 0$, $\frac{\Delta\rho^{\rm opt}}{\rho}$ is nonetheless slightly larger than the dc transport anisotropy for $T < T_s$. This disagreement might originate from a difference in the applied stress between the optical and dc transport measurements or from differences in scattering rate of samples used for the two types of measurements.

In order to highlight the optical anisotropy at high frequencies, we calculate the linear dichroism $\Delta\sigma_1(\omega)$, as defined in the introduction. For the purpose of further enhancing the optical anisotropy, we show in figure 8 $\widetilde{\Delta}\sigma_1(\omega, T)$, which is defined as $\Delta\sigma_1(\omega, T)$ from the MIR to the UV for $x = 0$, 0.025 and 0.045 at various temperatures after having subtracted its corresponding room temperature values and being appropriately normalized. The dichroism persists above T_N in the MIR range (figure 8), pairing our direct observations in terms of $R(\omega)$ and $\sigma_1(\omega)$ (figures 3 and 4). This representation highlights once more that the MIR feature moves towards lower frequencies upon increasing doping.

It is especially interesting to compare the temperature dependence of the dc ($\frac{\Delta\rho}{\rho}$) [10] and optical ($\Delta\sigma_1(\omega)$) anisotropy [18]. Two characteristic frequencies, identifying the position of the peaks in $\sigma_1(\omega)$ (figure 4), are selected in order to follow the temperature dependence of $\Delta\sigma_1(\omega)$; namely, $\omega_1 = 1500\,{\rm cm}^{-1}$ and $\omega_2 = 4300\,{\rm cm}^{-1}$ for $x = 0$; $\omega_1 = 1320\,{\rm cm}^{-1}$ and $\omega_2 = 5740\,{\rm cm}^{-1}$ for $x = 0.025$; $\omega_1 = 912\,{\rm cm}^{-1}$ and $\omega_2 = 5182\,{\rm cm}^{-1}$ for $x = 0.045$. It is remarkable that the temperature dependence of $\Delta\sigma_1(\omega)$ at ω_1 and ω_2 follows the temperature dependence of $\frac{\Delta\rho}{\rho}$ in all compounds (figure 7). $\Delta\sigma_1(\omega_i)$ ($i = 1, 2$) saturates at constant values well above T_s and then displays a variation for $T < 2T_s$. Here we first underscore that the rather pronounced optical anisotropy, extending up to temperatures higher than T_s for the stressed crystals, clearly implies an important pressure-induced anisotropy in the electronic structure, which is also revealed by ARPES measurements [6, 12].

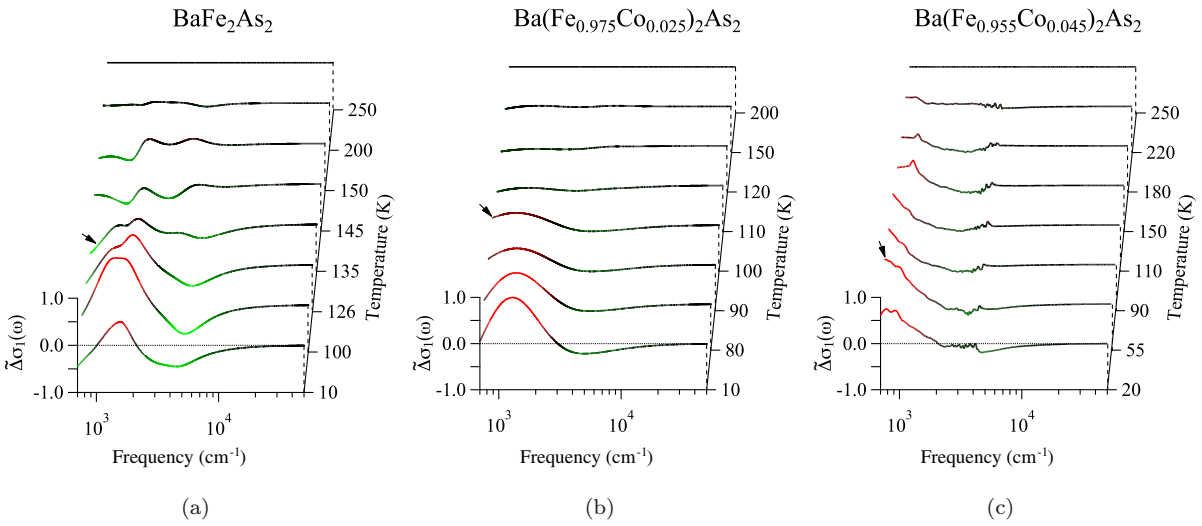

Figure 8. Temperature dependence of the normalized relative difference $\widetilde{\Delta}\sigma_1(\omega, T) = \Delta\sigma_1(\omega, T) - \Delta\sigma_1(\omega, 300\,\mathrm{K})$ of the optical dichroism of $BaFe_2As_2$ (a), $Ba(Fe_{0.975}Co_{0.025})_2As_2$ (b) and $Ba(Fe_{0.955}Co_{0.045})_2As_2$ (c). The black arrows indicate the $\Delta\sigma_1(\omega)$ at the temperature close to the structural phase transition at T_s. As color code: red marks positive, green negative values of $\widetilde{\Delta}\sigma_1(\omega, T)$.

Since the dichroism directly relates to a reshuffling of SW in $\sigma_1(\omega)$ in the overall FIR–NIR energy interval and more predominately in the MIR–NIR range (figure 4), $\Delta\sigma_1(\omega)$ at ω_1 is interrelated to that at ω_2 (i.e. the right y-axis for $\Delta\sigma_1(\omega_i)$ in figure 7 is inverted between ω_1 and ω_2), so that the behavior of $\Delta\sigma_1(\omega)$ is monotonic as a function of temperature and opposite in sign between ω_1 and ω_2 (figures 7 and 8). For $x = 0.025$ (figure 7) $\Delta\sigma_1(\omega_i) = 0$ at $T \gg T_s$. However, for $x = 0$ and 0.045, $\Delta\sigma_1(\omega_i)$ is found to be constant but apparently different from zero for $T \gg T_s$, which might reflect a systematic effect due to imperfect experimental conditions (e.g. too strong an applied uniaxial pressure). Nevertheless, the overall temperature dependence seems to behave in a very similar manner for all compositions. Significantly, the absolute variation of the dichroism across the transitions at selected frequencies is larger for $x = 0$ than for $x = 0.025$ and 0.045, contrary to the anisotropy in the dc resistivity [10]. Studying the doping dependence of the dichroism in a controlled pressure regime may help in excluding effects arising from different degrees of detwinning ($T < T_s$) and different magnitudes of induced anisotropy ($T > T_s$). Even so, it is encouraging that, contrary to the dc resistivity, the changes in the electronic structure appear to follow a similar trend to doping as the lattice orthorhombicity [14]. We might even conjecture that uniaxial pressure alters the structural parameters sensitively, such as the iron-pnictogen angle α [34]. Indeed, changes in α seem to induce relevant modifications in the shape of the Fermi surface and its nesting conditions as well as in its orbital makeup, which could imply consequences in terms of the superconducting order parameter, critical temperature and magnetic properties [34]. These latter issues remain, however, a theoretical challenge.

The origin of the orthorhombic transition has been discussed from the closely related perspectives of spin fluctuations (a so-called spin-induced nematic picture [35–38]) and also in terms of a more direct electronic effect involving, for instance, the orbital degree of freedom [27, 30, 31, 39–42]. In all cases one may expect some degree of electronic anisotropy.

While our findings do not allow us to uniquely single out a specific scenario, it is instructive to compare the observed dichroism with specific predictions made within models based on orbital order. The two well-defined energy scales ω_1 and ω_2 (figure 4) may represent optical transitions between states with the strongest d_{xz}/d_{yz} character, which are separated by about 0.3–0.4 eV. Such an energy splitting is indeed compatible with the theoretical calculations of the anisotropic optical conductivity [27] and of the linear dichroism in the x-ray absorption spectroscopy [31]. Nonetheless, the debate about the impact of orbital order on the electronic properties is far from being settled down, both experimentally and theoretically. Complementary to the discussion of the experimental findings sketched in the introduction and thoroughly summarized in [8], the understanding of the role of orbital ordering may benefit from a detailed comparison between infrared and Raman spectroscopy results. In this respect, it is worth mentioning that instead of the orbital ordering scenario a recent Raman scattering study [43] advocates a more conventional band-folding picture with two types of electronic transitions in the spin-density-wave state, where one type is eventually linked to the presence of Dirac cones in the electronic dispersion. On a more theoretical ground, Valenzuela *et al* [30] point out that for big values of orbital ordering the Drude weight anisotropy is less pronounced with respect to what is observed experimentally. Bascones *et al* [42] further establish a correlation between orbital ordering and magnetic super-exchange for the high-moment phase but not for the low-moment phase. While these latter calculations might be relevant at low temperatures, it remains to be seen how they can explain the onset of the anisotropy at/above T_s, where the spin symmetry is not yet broken.

We wish now to come back to the comparison between our optical results and the outcome of the LAPW calculations [19][5]. The model uses as initial lattice parameters those determined experimentally from the crystal structure of $BaFe_2As_2$ ($a = 5.6 \times 10^{-8}$, $c = 13.02 \times 10^{-8}$ cm and the arsenide Whyckoff position fixed at the experimental value of 0.354), but neglects the small orthorhombic distortion occurring at low temperatures. The magnetic ordering is modeled using a fixed striped phase, where stripes of spins up are alternated with stripes of spins down on each Fe plane, compatible with the magnetic configuration determined experimentally below T_N [4]. The destabilization of magnetism, induced above 6% Co-doping, was simulated by scaling the magnetic moment, calculated within the virtual crystal approximation [19], accordingly to the experimental critical temperature T_N [20]. The Co dopings calculated with this method reasonably agree within 5–10% with the experimental ones. This approach further corrects the deficiencies of the local spin density approximation. Therefore, the strategy in our approach consists in maintaining the lattice structure of the undoped configuration and in keeping the lattice fixed upon doping while reducing the magnetic moment.

Figure 9 shows the low-temperature measured (top panels) and calculated (bottom panels) optical conductivity for both the a- and b-axis and for the three dopings. For a direct comparison we have normalized all the measured and calculated $\sigma_1(\omega)$ to their respective maxima, thus obtaining $\tilde{\sigma}_1(\omega)$. The overall anisotropy of $\sigma_1(\omega)$ at low temperatures as well as the general features, such as the MIR (black arrows in figure 9) and NIR absorption bands, are fairly well caught by the calculation. There are, however, some differences: the experiment tends to display an MIR band along both directions, yet anisotropic (i.e. the shoulder on the low-frequency side of the NIR peak is well pronounced for $x = 0$ and $x = 0.045$ and appears as a broad tail for $x = 0.025$), while in the calculation this latter band is absent along the b-axis.

Focusing on the similarities between theory and experiment, we may state that the predictions of the enhancement of the MIR band and the metallic contribution of $\sigma_1(\omega)$ in

[5] The ELK code at http://elk.sourceforge.net/ was employed for the calculations.

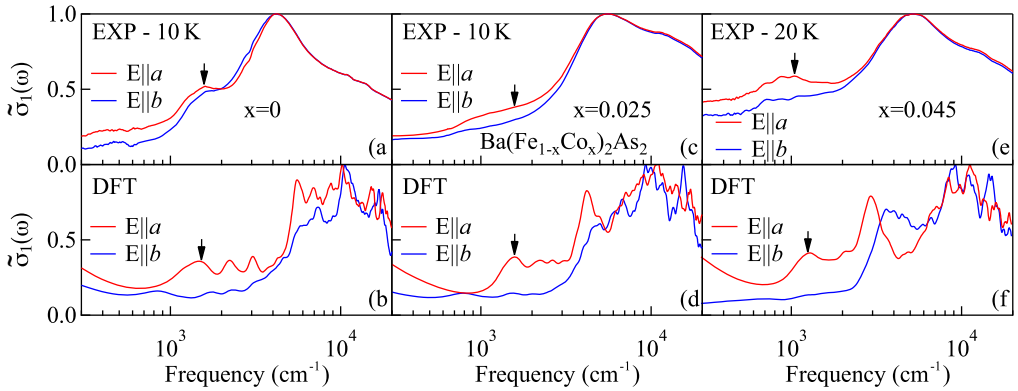

Figure 9. Normalized optical conductivity $\tilde{\sigma}_1(\omega)$ of $BaFe_2As_2$ (a, b), $Ba(Fe_{0.975}Co_{0.025})_2As_2$ (c, d), and $Ba(Fe_{0.955}Co_{0.045})_2As_2$ (e, f) measured (top panels) at the lowest temperatures with light polarized along the *a*- and *b*-axis and obtained by DFT calculations (bottom panels) along the antiferromagnetically oriented spins and parallel to the ferromagnetic stripes [19]. The black arrows indicate the MIR band in the measurements and calculations.

the FIR range along the *a*-direction and their depletion along the *b*-direction are fairly close to the experimental findings. Moreover, the center of the calculated MIR band (black arrows in figure 9, bottom panels) shifts at lower frequencies for increasing dopings, which also mimics the data.

The MIR band is linked to the modeled magnetic stripe configuration which was shown to correspond to the energy-minimum configuration of these systems [19]. Therefore, the DFT calculation strongly supports a 'magnetic origin' of the MIR band, which would originate from the Fermi topology reconstruction in the magnetically ordered state. In this scenario, one would reasonably expect that the MIR band disappears above the magnetic phase transition, contrary to our observations. However, a dynamic antiferromagnetic order due to spin fluctuations could persist in the paramagnetic phase well above the phase transition temperature [44]. The fingerprints of such underlying spin fluctuations would be frozen to fast enough probes as optics, thus explaining the persistence above the phase transition of the MIR band in our spectra.

Finally, we comment on the comparison at higher (NIR) frequencies, where the agreement between calculation and experiment is less precise, possibly because of the finite *k*-point sampling. The major interband peak of $\tilde{\sigma}_1(\omega)$ experimentally observed at about 5000 cm^{-1} is only roughly reproduced by and is shifted to slightly higher frequencies in the theoretical calculations. Furthermore, the NIR feature shows a steeper rise in the DFT calculations than in the experiment. It seems that spin-polarized DFT calculations require a smaller renormalization factor with respect to unpolarized ones in order to account for the relative frequency shifts between calculated and experimental spectra. This latter issue is intensively debated in the literature, as far as the twinned samples are concerned (for a review with additional references, see [45, 46]). A thorough discussion of correlation, combined with the electronic anisotropy and leading to renormalization effects of the band structure, is at this stage too premature as well as too speculative, calling for more theoretical investigations.

5. Conclusions

The charge dynamics of detwinned $Ba(Fe_{1-x}Co_x)_2As_2$ single crystals in the underdoped regime reveals an in-plane temperature and doping-dependent optical anisotropy. At low frequencies the optical measurements offer the unique opportunity to disentangle the distinct behaviors of the Drude weights and scattering rates of the itinerant charge carriers, which are both enhanced along the antiferromagnetic a-axis with respect to the ferromagnetic b-axis. Our findings on such single-domain specimens allow us to shed light on the counterintuitive anisotropic behavior ($\rho_b > \rho_a$) of the dc resistivity. The dc anisotropy below T_N is principally determined by the anisotropy in the low-frequency Drude weight (i.e. changes in the electronic structure close to the Fermi energy), outweighing the non-negligible anisotropy of the scattering rates between the a- and b-axis. Understanding whether the resistivity anisotropy above T_N originates from the Fermi surface, perhaps due to the difference in orbital occupancy as revealed by ARPES [27, 31], or from anisotropic scattering, perhaps associated with incipient spin fluctuations [33], remains an open issue. The current optical data may be in partial agreement with both points of view, thus motivating further experiments in order to definitely address the origin of the anisotropy above T_N for the dc limit of the optical response.

The optical anisotropy extends to relatively high frequencies and temperatures above the phase transitions for crystals held under uniaxial stress. The resulting linear dichroism reveals the electronic nature of the structural transition and implies a substantial nematic susceptibility, which would also agree with the strong decrease of the shear modulus (proportional to the inverse of the nematic susceptibility) [37].

The interplay of magnetism and Fermi surface topology was then elaborated through a comparison of our optical measurements with theoretical calculations obtained from DFT within the full-potential LAPW method. The calculations are able to consistently track the large in-plane anisotropy of the optical response and its doping dependence and allow us to ascribe the MIR band located at about 1500 cm^{-1} to antiferromagnetic ordered stripes.

Acknowledgments

The authors acknowledge fruitful discussions with B Valenzuela, S Kivelson, T Devereaux, C Homes, D N Basov, R M Fernandes, J Schmalian, W Lv and D Lu and valuable help by J Johannsen in collecting part of the data. This work has been supported by the Swiss National Foundation for Scientific Research within the NCCR MaNEP pool. This work was also supported by the Department of Energy, Office of Basic Energy Sciences under contract no. DE-AC02-76SF00515. The work in Cagliari was supported by the Italian MIUR through PRIN2008XWLWF.

References

[1] Norman M R 2011 *Science* **332** 196 and references therein
[2] Basov D N and Chubukov A V 2011 *Nat. Phys.* **7** 272 and references therein
[3] Johnson D C 2010 *Adv. Phys.* **59** 803 and references therein
[4] Li H-F *et al* 2010 *Phys. Rev.* B **82** 140503(R)
[5] Chuang T-M *et al* 2010 *Science* **327** 181
[6] Wang Q *et al* 2010 arXiv:1009.0271 (unpublished)

[7] Terashima T *et al* 2011 *Phys. Rev. Lett.* **107** 176402
[8] Fisher I A, Degiorgi L and Shen Z X 2011 *Rep. Prog. Phys.* **74** 124506 and references therein
[9] Tanatar M A *et al* 2009 *Phys. Rev.* B **79** 180508(R)
[10] Chu J-H *et al* 2010 *Science* **329** 824
[11] Chu J-H *et al* 2010 *Phys. Rev.* B **81** 214502
[12] Yi M *et al* 2011 *Proc. Natl. Acad. Sci. USA* **108** 6878
[13] Kim Y *et al* 2011 *Phys. Rev.* B **83** 064509
[14] Prozorov R *et al* 2009 *Phys. Rev.* B **80** 174517
[15] Tanatar M A *et al* 2010 *Phys. Rev.* B **81** 184508
[16] Blomberg E C *et al* 2011 *Phys. Rev.* B **83** 134505
[17] Kuo H-H *et al* 2011 *Phys. Rev.* B **84** 054540
[18] Dusza A *et al* 2011 *Europhys. Lett.* **93** 37002
[19] Sanna A *et al* 2011 *Phys. Rev.* B **83** 054502
[20] Chu J-H *et al* 2009 *Phys. Rev.* B **79** 014506
[21] Lester C *et al* 2009 *Phys. Rev.* B **79** 144523
[22] Dressel M and Grüner G 2002 *Electrodynamics of Solids* (Cambridge: Cambridge University Press)
[23] Lucarelli A *et al* 2010 *New J. Phys.* **12** 073036 and references therein
[24] Nakajima M *et al* 2011 *Proc. Natl. Acad. Sci. USA* **108** 12238
[25] Yin Z P *et al* 2011 *Nat. Phys.* **7** 294
[26] Sugimoto K *et al* 2011 *J. Phys. Soc. Japan* **80** 033706
[27] Lv W and Phillipps P 2011 *Phys. Rev.* B **84** 174512
[28] Benfatto L *et al* 2011 *Phys. Rev.* B **83** 224514
[29] Wu D *et al* 2010 *Phys. Rev.* B **81** 100512(R) and references therein
[30] Valenzuela B *et al* 2010 *Phys. Rev. Lett.* **105** 207202
[31] Chen C-C *et al* 2010 *Phys. Rev.* B **82** 100504(R)
[32] Turner A M *et al* 2009 *Phys. Rev.* B **80** 224504
[33] Fernandes R M *et al* 2011 *Phys. Rev. Lett.* **107** 217002
[34] Calderón M J *et al* 2009 *Phys. Rev.* B **80** 094531
[35] Xu C, Müller M and Sachdev S 2008 *Phys. Rev.* B **78** 020501(R)
[36] Johannes M D and Mazin I 2009 *Phys. Rev.* B **79** 220510(R)
[37] Fernandes R M *et al* 2010 *Phys. Rev. Lett.* **105** 157003
[38] Fradkin E *et al* 2010 *Annu. Rev. Condens. Matter Phys.* **1** 153 and references therein
[39] Krüger F *et al* 2009 *Phys. Rev.* B **79** 054504
[40] Lee C-C *et al* 2009 *Phys. Rev. Lett.* **103** 267001
[41] Lv W *et al* 2010 *Phys. Rev.* B **82** 045125
[42] Bascones E, Calderón M J and Valenzuela B 2010 *Phys. Rev. Lett.* **104** 227201
[43] Chauviere L *et al* 2011 *Phys. Rev.* B **84** 104508
[44] Mazin I I and Johannes M D 2009 *Nat. Phys.* **5** 141
[45] Qazilbash M M *et al* 2009 *Nat. Phys.* **5** 647
[46] Degiorgi L 2011 *New J. Phys.* **13** 023011